



# The effects of hydrothermal temperature and time on structure and magnetic properties of lanthanum-substituted zinc ferrites

Tengyan Wu<sup>1,2</sup> · Duxin Li<sup>1</sup> · Menglin Wei<sup>1</sup> · Hao Han<sup>1</sup>

Received: 26 October 2018 / Accepted: 18 January 2019 / Published online: 11 March 2019  
© Springer-Verlag GmbH Germany, part of Springer Nature 2019

## Abstract

The  $\text{ZnFe}_2\text{O}_4$  and  $\text{ZnLa}_{0.5}\text{Fe}_{1.5}\text{O}_4$  zinc ferrites had been prepared by the hydrothermal method. The detection method using in this investigation was X-ray diffraction, scanning electronic microscope, Fourier transformed infrared spectrometer (FTIR), and vibrating sample magnetometer. The results indicated that the samples had spinel structures. This study revealed that the crystallite size, lattice constant, and X-ray density of samples were decreased, while prolonged holding time and increased temperature, whereas the crystallite size was increased with the temperature increasing. Four absorption bands were observed in FTIR spectra and assigned to the corresponding site bonds. The saturation magnetization ( $M_S$ ), coercivity, magnetic moment, and anisotropy constant ( $K$ ) were affected by the holding time and temperature. Anisotropy constant proved dependence on the temperature, and it increased with the enhancement of temperature.

## 1 Introduction

Cancer diseases and cardiovascular are the two leading causes of death worldwide. In the present, cancer is commonly treated by the combination of surgery, radiation therapy, and chemotherapy. However, surgical treatment is only suitable for patients with tumors which have not yet metastasized, and chemotherapy kills normal cells as well as cancerous. These side effects have great limitation in their application. Magnetic nanoparticles (MNPs) are perceived as promising materials for magnetic resonance imaging agents, biomedical drug carriers, magnetic hyperthermia [1–3], etc, due to their superior magnetic properties and high specific surface. MNPs can also be targeted to tumor site in a magnetic field, which had importance in cancer therapy [4]. In this regard, MNPs have shown great potential in targeted drug delivery for cancer treatment [5]. For example, in magnetically targeted drug delivery, carriers comprising

of coated MNPs loaded with anti-cancer drug are injected into the patient body via the human circulatory system, or are able to transport pharmaceuticals to a specific site in the body when facilitated by an external magnetic field [6, 7]. The latter, it can prolong the drug at the relevant cells, and more concentrated doses of drug. The researches on the MNPs of crystallite size, morphology, magnetic properties, and biocompatibility have become an attractive field of biomaterial in recent years. Researchers studied on homogeneity particle size and size distribution, morphology, and agglomerate size of the most important parameters in MNPs by the synthesis process of MNPs [8–10], different transition metal cations [11–13], surface modification technology of material [14, 15], and has yielded the certain result. Zhang et al. found that grain size and maximum magnetization increased with the increasing sintering temperature and Yang et al. found that  $H_c$  and  $M_S$  varied with increasing sintering temperature [16, 17], MNPs were coated with multifunction polymers that can be used to improve the agglomeration and reduce the side effects on normal cells and tissues [18, 19]. Some experiments demonstrate that long-lasting hyperthermia could effectively induce the apoptosis of tumor cells, and finally suppress the tumor growth within a certain period of time [19–21].

The research background of this paper is based on the preparation of zinc ferrites magnetic materials for tumor therapy by magnetic hyperthermia. Based on the works in the literature, research of size, morphology, and magnetic

✉ Duxin Li  
liduxin@csu.edu.cn

<sup>1</sup> State Key Laboratory of Powder Metallurgy, Central South University, Changsha 410083, China

<sup>2</sup> Hunan Provincial Key Laboratory of Fine Ceramics and Powder Materials, School of Materials and Environmental Engineering, Hunan University of Humanities, Science and Technology, Loudi 417000, Hunan, China

properties for  $\text{ZnFe}_2\text{O}_4$  ferrites was studied with different prepared methods. Some researchers reported that induces structural modification as well as improvement in magnetic properties by the introduction of rare-earth elements [22, 23]. However, at present, there were no detailed articles about lanthanum (La)-doped zinc ferrites magnetic were synthesis by hydrothermal, which intrigued by our interest to prepared samples of  $\text{ZnLa}_{0.5}\text{Fe}_{1.5}\text{O}_4$  by hydrothermal. The  $\text{ZnFe}_2\text{O}_4$  and  $\text{ZnLa}_{0.5}\text{Fe}_{1.5}\text{O}_4$  zinc ferrites had been prepared through hydrothermal method on the condition of the diverse parameters, and the influence of temperature and holding time on microstructure and magnetic properties of zinc ferrites was studied.

## 2 Experimental details

$\text{ZnFe}_2\text{O}_4$  and  $\text{ZnLa}_{0.5}\text{Fe}_{1.5}\text{O}_4$  zinc ferrites were synthesized by hydrothermal method.  $\text{FeCl}_3 \cdot 6\text{H}_2\text{O}$  (ferric chloride),  $\text{La}(\text{NO}_3)_3 \cdot 6\text{H}_2\text{O}$  (lanthanum nitrate), and  $\text{ZnCl}_2$  (zinc chloride) were used as the starting chemical reagents without any further purification for the synthesis. Aqueous solutions of ferric chloride, zinc chloride, and lanthanum nitrate are prepared by adding 40 ml of deionized water and all the solutions were added and mixed thoroughly using a magnetic stirrer for 30 min, and 0.25 ml of NaOH of 2 mol/l was dropwised into the previous solution under stirring continuously at room temperature, until the pH of the solution stabilized 10. After tending a stable pH value, after some time of inactivity, the upper clear liquid was removed, and the remnant mixture was transferred to Teflon lined sealed stainless steel autoclaves and kept inside an oven for 12 h at different temperatures, 170 °C, 180 °C, 200 °C, respectively, and maintained at 180 °C for 10 h, 11 h, and 13 h, respectively. The autoclave was taken from the oven and natural cooling to room temperature. Then, the sample was washed thoroughly three times using by deionized water and anhydrous ethanol, respectively, and the sample dried in the oven for 24 h at a temperature of 80 °C was obtained the dried sample. The dried sample was grinded in a mortar and pestle until fine powder of  $\text{ZnFe}_2\text{O}_4$  and  $\text{ZnLa}_{0.5}\text{Fe}_{1.5}\text{O}_4$  was obtained.

Techniques such as X-ray diffraction (XRD), Fourier transformed infrared spectrometer (FTIR), scanning electronic microscope (SEM), and vibrating sample magnetometer (VSM) were used to characterize the prepared  $\text{ZnFe}_2\text{O}_4$  and  $\text{ZnLa}_{0.5}\text{Fe}_{1.5}\text{O}_4$  nanoferrites at room temperature. For all the samples, the XRD powder patterns were recorded on Rigaku D/max 2550 diffractometer using the  $\text{Cu K}\alpha$  as radiation source to analyze the prepared samples as the  $2\theta$  position from 20° to 80°. The functional groups and chemical bonds existing in prepared samples were identified on Nicolet iS10 spectra in the wavenumber range of

4000–400  $\text{cm}^{-1}$ . A pellet was created of 95% KBr with 5% prepared nanoferrites for FTIR spectral analysis. The morphology microstructures were investigated with a QUANTA 650FEG scanning electronic microscope (SEM). Magnetic measurements of prepared samples were performed using a PPMS-9VSM with an applied magnetic field of –15 kOe to 15 kOe.

## 3 Results and discussion

### 3.1 XRD analysis

Figure 1 shows the XRD spectra of the samples of  $\text{ZnFe}_2\text{O}_4$  and  $\text{ZnLa}_{0.5}\text{Fe}_{1.5}\text{O}_4$  at 180 °C with different holding times, and Fig. 2 shows the XRD spectral of the samples of  $\text{ZnLa}_{0.5}\text{Fe}_{1.5}\text{O}_4$  for 12 h with different temperatures, respectively. The main reflection planes (220), (311), (400), (422), (511), and (440) are appeared in Figs. 1 and 2, which matched well with the JCPDS date (#22-1012). However, for the sample at 200 °C, some less intense impurity phases were found in XRD spectra, which matched well with the JCPDS date (#36-1481). The result indicated that  $\text{La}(\text{OH})_3$  was existence. The reason may be higher doping concentration and leads to the increase of potential barrier for  $\text{La}^{3+}$  ion to enter into spinel crystal lattice. Consequently, a small amount of  $\text{La}^{3+}$  was remained, and  $\text{La}(\text{OH})_3$  was formation. Besides,  $\text{La}^{3+}$  ion-substituted zinc ferrites ( $\text{ZnLa}_{0.5}\text{Fe}_{1.5}\text{O}_4$ ) nanoparticles had a stronger diffraction intensity and sharp diffraction, compared with zinc ferrite ( $\text{ZnFe}_2\text{O}_4$ ). The results indicated that crystallite size of  $\text{ZnLa}_{0.5}\text{Fe}_{1.5}\text{O}_4$  was larger than crystallite size of  $\text{ZnFe}_2\text{O}_4$ , which may be due to the substitution of relatively smaller

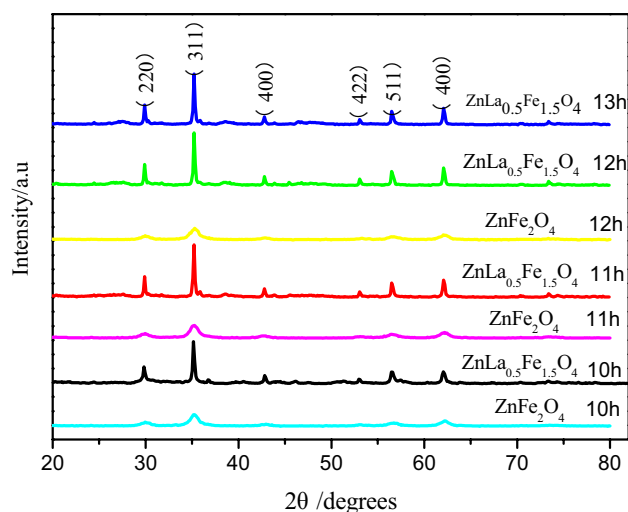


**Fig. 1** Powder XRD date for  $\text{ZnLa}_{0.5}\text{Fe}_{1.5}\text{O}_4$  and  $\text{ZnFe}_2\text{O}_4$  with different holding times at 180 °C

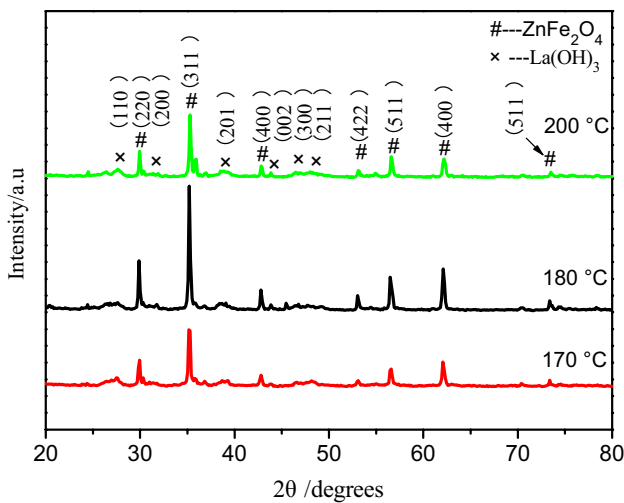


**Fig. 2** Powder XRD date for  $\text{ZnLa}_{0.5}\text{Fe}_{1.5}\text{O}_4$  with different temperatures

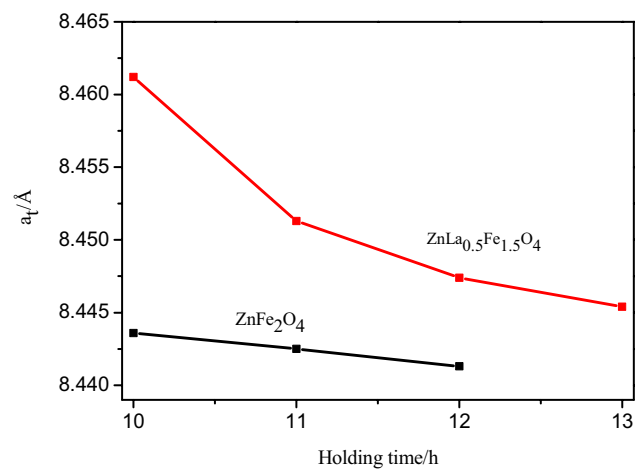
ionic radius size Fe (0.64 Å) ions with larger ionic radius La (1.06 Å) ions. It was also verified that crystallite size of the samples was calculated using Scherrer formula [24], and the results are given in Table 1.

The lattice constant  $a_t$  was calculated using the software and further confirmed by the following relation [25], and the results are given in Table 1.

The X-ray density for all composition was calculated [26], the results are given in Table 1.

Based on the data in Table 1,  $\rho_{\text{X-ray}}$  of  $\text{ZnFe}_2\text{O}_4$  and  $\text{ZnLa}_{0.5}\text{Fe}_{1.5}\text{O}_4$  at 180 °C increased, while increasing holding time, it was due to a reduction in volume.

Figure 3 displays variation of true lattice constant  $a_t$  against holding time. It showed that lattice constant  $a_t$  of  $\text{ZnFe}_2\text{O}_4$  and  $\text{ZnLa}_{0.5}\text{Fe}_{1.5}\text{O}_4$  decreased with increasing holding time, which was in good agreement with the literature [27]. It can also be seen that the lattice constant  $a_t$  of  $\text{ZnLa}_{0.5}\text{Fe}_{1.5}\text{O}_4$  was greater than that of  $\text{ZnFe}_2\text{O}_4$ , it may be rare earth of La ion getting substituted in the lattice [28].



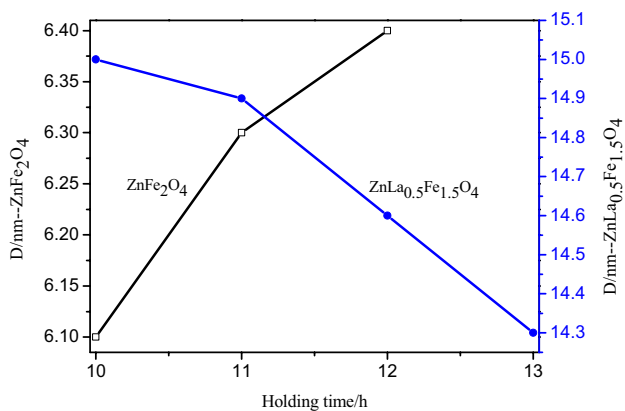
**Fig. 3**  $\text{ZnLa}_{0.5}\text{Fe}_{1.5}\text{O}_4$  and  $\text{ZnFe}_2\text{O}_4$  of lattice constant  $a_t$  with different holding times at 180 °C

Figure 4 shows  $\text{ZnLa}_{0.5}\text{Fe}_{1.5}\text{O}_4$  and  $\text{ZnFe}_2\text{O}_4$  of crystallite size with different holding times at 180 °C. According to the Ostwald Ripening theory [29], extending the holding time can effectively promote the crystallite size growth, this explained that crystallite size of  $\text{ZnFe}_2\text{O}_4$  increases with the increasing holding time. Nevertheless, crystallite size of  $\text{ZnLa}_{0.5}\text{Fe}_{1.5}\text{O}_4$  decreased with the increasing of holding time. The reason was maybe that mismatch of small size  $\text{Fe}^{3+}$  (0.64 Å) ion was substituted by large size  $\text{La}^{3+}$  (1.06 Å) and formed the crystalline anisotropy, which led to the creation of volume strain of the crystallite with holding time increasing [30]. The crystallite size decreased with prolonging holding time, which led to the volume strain relaxed, and balanced between volume strain and crystal anisotropy was achieved [11].

Figure 5 displays both the crystallite size  $D$  increased and true lattice constant  $a_t$  against temperature risen. It was worth to note that the crystallite size was strongly affected by the temperature. Higher temperature resulted the more

**Table 1** Lattice constant  $a_t$ , crystallite size  $D$ , cell volume  $V$  and X-ray density of  $\text{ZnLa}_{0.5}\text{Fe}_{1.5}\text{O}_4$  and  $\text{ZnFe}_2\text{O}_4$

Composition	Temperature (°C)	Holding time (h)	Lattice constant, $a_t$ (Å)	Crystallite size, $D$ (nm)	Volume (Å <sup>3</sup> )	X-ray density $\rho_{\text{X-ray}}$ (g/cm <sup>3</sup> )
$\text{ZnFe}_2\text{O}_4$	180	10	8.4436	6.1	601.98	5.3195
$\text{ZnFe}_2\text{O}_4$	180	11	8.4425	6.3	601.74	5.3230
$\text{ZnFe}_2\text{O}_4$	180	12	8.4413	6.4	601.49	5.3250
$\text{ZnLa}_{0.5}\text{Fe}_{1.5}\text{O}_4$	180	10	8.4612	15.0	605.75	5.4218
$\text{ZnLa}_{0.5}\text{Fe}_{1.5}\text{O}_4$	180	11	8.4513	14.9	603.63	5.4409
$\text{ZnLa}_{0.5}\text{Fe}_{1.5}\text{O}_4$	180	12	8.4474	14.6	602.79	5.4485
$\text{ZnLa}_{0.5}\text{Fe}_{1.5}\text{O}_4$	180	13	8.4454	14.3	602.37	5.4523
$\text{ZnLa}_{0.5}\text{Fe}_{1.5}\text{O}_4$	170	12	8.4513	13.7	603.63	5.4409
$\text{ZnLa}_{0.5}\text{Fe}_{1.5}\text{O}_4$	200	12	8.4440	16.1	602.07	5.4550



**Fig. 4** ZnLa<sub>0.5</sub>Fe<sub>1.5</sub>O<sub>4</sub> and ZnFe<sub>2</sub>O<sub>4</sub> of crystallite size with different holding times at 180 °C

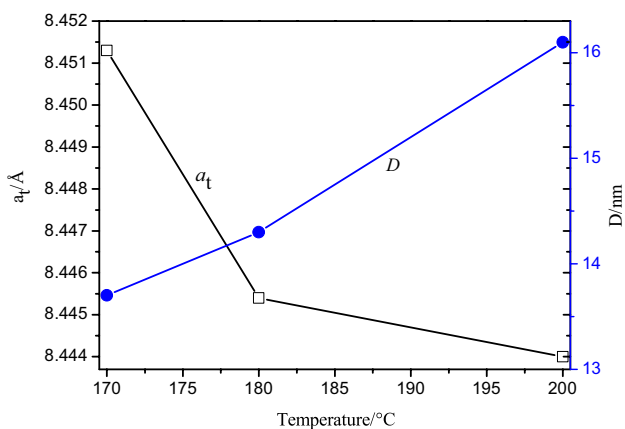
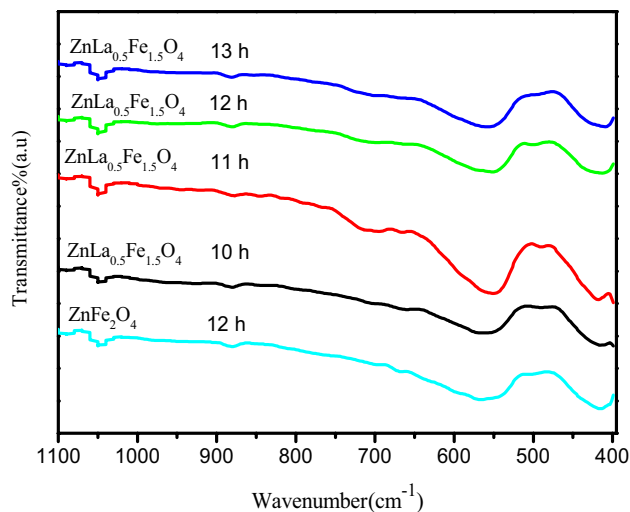


**Fig. 5** ZnLa<sub>0.5</sub>Fe<sub>1.5</sub>O<sub>4</sub> of lattice constant *a<sub>t</sub>* and crystallite size *D* with different temperatures

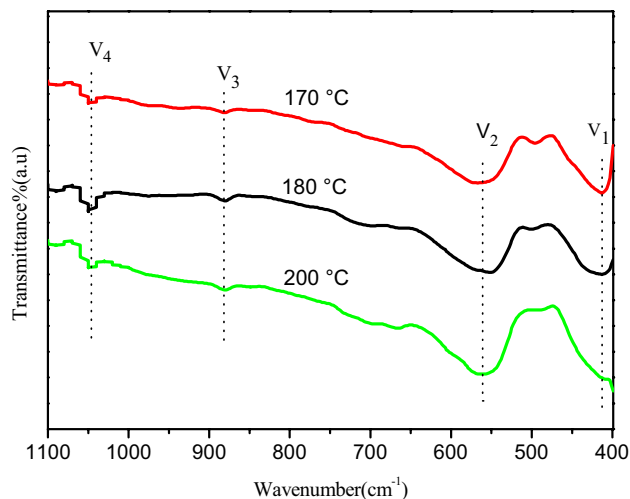
vapor pressure in the Teflon reactor and the greater pressure on the crystal cells, which limited the growth of crystal cell and reduced the lattice constant *a<sub>t</sub>*. However, for crystallite size, the increasing rate of nucleation rate was slower than that of crystal growth rate as temperature increasing and the granularity of crystallite size was bigger. Another reason was the higher probability of crystallite collision with higher the temperature, which was prone to form large-scale particles.

### 3.2 FTIR spectroscopy

The FTIR spectrum of the prepared ZnLa<sub>0.5</sub>Fe<sub>1.5</sub>O<sub>4</sub> nanoferrites is shown in Figs. 6 and 7. The FTIR spectrum of Fig. 6 indicated that ZnLa<sub>0.5</sub>Fe<sub>1.5</sub>O<sub>4</sub> and ZnFe<sub>2</sub>O<sub>4</sub> were basically consistent. It indicated that La<sup>3+</sup> successfully replaces Fe<sup>3+</sup> and enters the lattice without changing the crystal structure. The FTIR spectrum showed two absorption bands which were the characteristic absorption bands



**Fig. 6** FTIR spectra of the prepared ZnLa<sub>0.5</sub>Fe<sub>1.5</sub>O<sub>4</sub> nanoferrites with different holding times

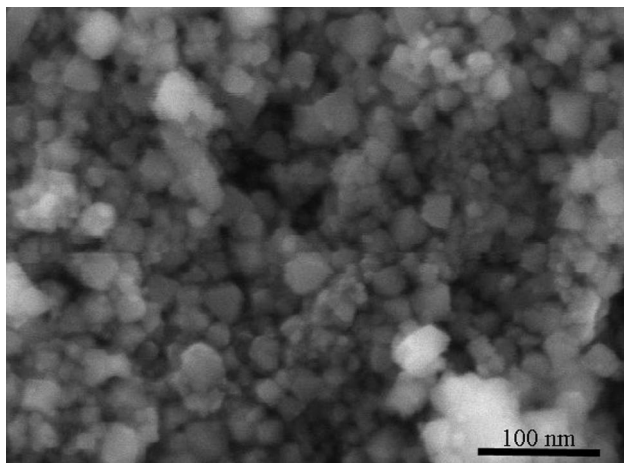


**Fig. 7** FTIR spectra of the prepared ZnLa<sub>0.5</sub>Fe<sub>1.5</sub>O<sub>4</sub> nanoferrites with different temperatures

of spine nanoferrites. The lower frequency absorption band  $\nu_1$  lied in around 420  $\text{cm}^{-1}$ , corresponding to the band that was the intrinsic stretching vibration of the between the oxygen ion and octahedral site metal ion (Fe–O). Higher frequency absorption band  $\nu_2$  lied in around 560  $\text{cm}^{-1}$ , corresponding to the band that was the intrinsic stretching vibration of the between the oxygen ion and tetrahedral site metal ion (Zn–O) [31]. Compared to the values of  $\nu_1$ , the values of  $\nu_2$  were higher. Because of the normal mode in ferrite spine, the vibration of the octahedral cluster was lower than that the tetrahedral cluster for the shorter bond length of the tetrahedral (Zn<sup>2+</sup>) clusters than that of the octahedral (Fe<sup>3+</sup>) clusters [32,

**Table 2** EDS pattern of the sample at temperature 180 °C and holding time 10 h

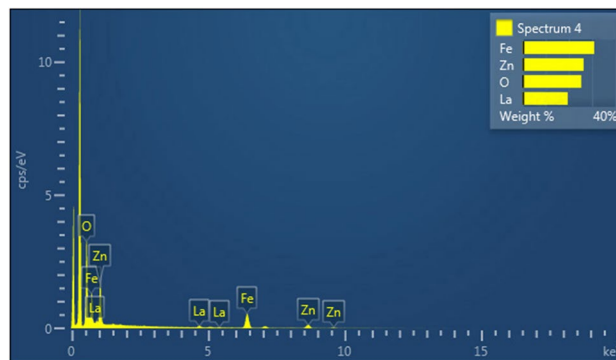
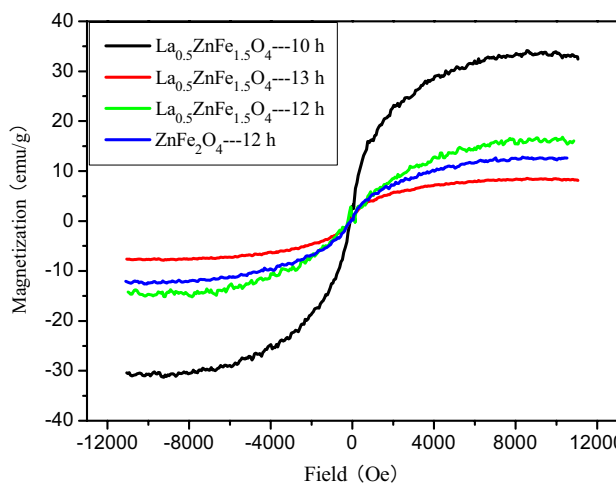
Element types	O (%)	Fe (%)	Zn (%)	La (%)
Theoretical weight%	22.65	29.62	23.15	24.58
EDS	24.09	31.49	24.73	19.69

**Fig. 8** SEM image of the  $\text{ZnLa}_{0.5}\text{Fe}_{1.5}\text{O}_4$  nanoparticles at temperature 180 °C and holding time 10 h

33]. Besides, the two weak absorption bands of  $\nu_3$  and  $\nu_4$  were observed in the FTIR spectra, which were in around  $880\text{ cm}^{-1}$ , and  $1050\text{ cm}^{-1}$ , respectively. Divalent ions  $\text{Zn}^{2+}$  in the A-sites led to the band  $\nu_3$  generation [34]. The presence of complexes  $\text{Fe}^{4+}\text{-O}^{2-}$  and/or  $\text{La}^{4+}\text{-O}^{2-}$  was duo to the band  $\nu_4$  assigned to the tetravalent metal ion-oxygen. The electron hopping between the  $\text{La}^{3+}$  and  $\text{Fe}^{3+}$  ions may cause the tetravalent ions of  $\text{La}^{4+}$  and  $\text{Fe}^{4+}$  produce [35–37].

### 3.3 Morphology characterization

The morphology of  $\text{ZnLa}_{0.5}\text{Fe}_{1.5}\text{O}_4$  for the temperature 180 °C and holding time 10 h was observed by SEM. Figure 8 shows the SEM image of  $\text{ZnLa}_{0.5}\text{Fe}_{1.5}\text{O}_4$  sample. The Nano measurer software was used to calculate the particle size. The average particle size of the sample was 19 nm, which was approximate with the Scherrer formula result (15 nm). In addition, EDS analyses showed that the sample was composed of O, Fe, Zn, and La elements. As shown in Table 2, the elements of EDS analyses were close to the stoichiometric ration. These results indicated that  $\text{La}^{3+}$  ions were successfully introduced into the zinc ferrites (Fig. 9).

**Fig. 9** Elemental analysis by EDS spectrum of the  $\text{ZnLa}_{0.5}\text{Fe}_{1.5}\text{O}_4$  nanoparticles at temperature 180 °C and holding time 10 h**Fig. 10** Hysteresis loops for  $\text{ZnLa}_{0.5}\text{Fe}_{1.5}\text{O}_4$  samples at 180 °C with different holding times

### 3.4 Magnetic analysis

The obtained magnetic hysteresis loops by VSM for the as-prepared  $\text{ZnLa}_{0.5}\text{Fe}_{1.5}\text{O}_4$  nano-ferrite samples at different holding times and different temperatures are shown in Figs. 10 and 11, respectively. The values of saturation magnetization ( $M_S$ ) for all samples at different holding times and different temperatures are listed in Table 3. Results depicted that the curves have a small coercivity and saturation magnetization, which was characteristic of the soft magnetic materials.

Figure 10 shows that the saturation magnetization value of the prepared  $\text{ZnLa}_{0.5}\text{Fe}_{1.5}\text{O}_4$  nanoferrite was 34, 16.0, and 4.7 emu/g at different holding times, 10 h, 12 h, and 13 h, respectively. The saturation magnetization for the samples decreased with increasing the holding time. In the previous XRD analysis, we had already known that crystallite size of  $\text{ZnLa}_{0.5}\text{Fe}_{1.5}\text{O}_4$  decreased with increasing holding

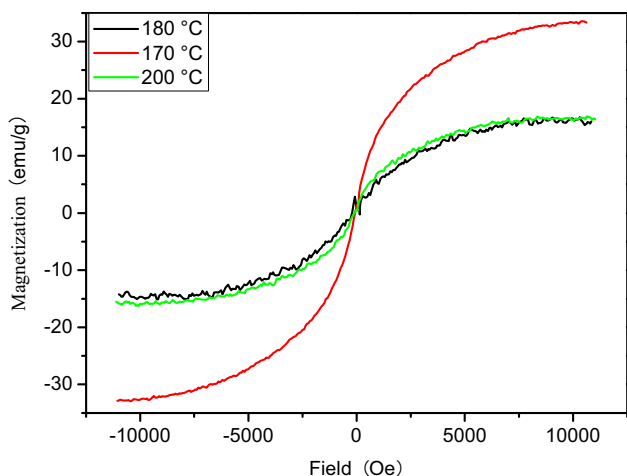


**Fig. 11** Hysteresis loops for ZnLa<sub>0.5</sub>Fe<sub>1.5</sub>O<sub>4</sub> samples at 12 h with different temperatures

time. With holding time prolonging, the crystallite size of the samples decreased, which increased the surface effect [30]. The structure at the surface is distorted and the atoms on the surface are strained to produce various interatomic spacing, low coordination numbers, and vacancies which in turn breaks the exchange bonds of the surface atoms leading to spin disorder [38]. Crystallite size of the sample decreased due to increase holding time, and decreasing crystallite size led to the increase of spins disordering which resulted in the reduction of saturation magnetization. Besides, Fig. 10 shows that the saturation magnetization value of the prepared ZnLa<sub>0.5</sub>Fe<sub>1.5</sub>O<sub>4</sub> ( $D = 14.6$  nm) and ZnFe<sub>2</sub>O<sub>4</sub> ( $D = 6.4$  nm) was 16 and 13 emu/g, respectively. It can be found that the influence of crystallite size on saturation magnetization was not significant. The observed behavior could be attributed to the factors: In the spinel ferrite, the saturation magnetization is dominated by the super-exchange interactions between the tetrahedral (Zn-sites) and octahedral (Fe-sites) sites cations. La<sup>3+</sup> ions were not magnetic, because La<sup>3+</sup> ions were zero magnetic moment, and La<sup>3+</sup> ions do not take part in the exchange interactions to the nearest neighboring ions. Hence, it will decrease the number of magnetic linkages occurring between tetrahedral and octahedral cations.

Figure 11 shows that the  $M_S$  value of the prepared ZnLa<sub>0.5</sub>Fe<sub>1.5</sub>O<sub>4</sub> nanoferrite was 35, 16.0, and 16.2 emu/g at different temperatures, 170 °C, 180 °C, and 200 °C, respectively. Results showed that saturation magnetization of the sample at 170 °C was higher compared with the samples at 180 °C and 200 °C. The observed behavior could be attributed to two the factor: the irregularity of magnetic moment arrangement in crystal increased with the advance of temperature in action. Thus, the value of saturation magnetization was reduced. On the other hand, with increasing temperature, the crystallite size of the samples increased, and increasing crystallite size led to the decrease of spins disordering which resulted in the increase of saturation magnetization. These two factors cause the saturation magnetization value changes up and down randomly.

The values of coercivity for the samples for different holding times at 180 °C are listed in Table 3. The coercivity of the samples increased, while the holding time prolong. It could be due to the presence of magnetic multi-domain in the sample. In the multi-domain region, the variation of coercivity with the crystallite size can be expressed as the following equation [30]:

$$H_C = e + \frac{f}{D}, \tag{1}$$

where ‘ $e$ ’ and ‘ $f$ ’ are constants and ‘ $D$ ’ is the crystallite size.

Hence, the coercivity increases, as the crystallite size decreases in the multi-domain region.

However, we have observed that coercivity increased with the temperature (crystallite size increase with the increase temperature). It may be formula single domain at particular temperature (170 °C and 200 °C). In a single domain region, the variation of coercivity with the crystallite size was expressed as the equation [30]:

$$H_C = g - \frac{h}{D^2}, \tag{2}$$

where  $g$  and  $h$  are constant. Hence, coercivity increases with the increase in crystallite size in the single domain region.

The magnetic moment  $n_B$  per atom in Bohr magneton units ( $\mu_B$ ) could be calculated using the following relation [39]:

**Table 3** Saturation magnetization ( $M_S$ ), coercivity ( $H_c$ ), remnant magnetization ( $M_r$ ), magnetic moment ( $n_B$ ), and anisotropy constant ( $K$ )

Composition	Temperature (°C)	Holding time (h)	$M_S$ (emu/g)	$M_r$ (emu/g)	$H_c$ (Oe)	$n_B$ ( $\mu_B$ )	$K$ (erg/Gauss)
ZnLa <sub>0.5</sub> Fe <sub>1.5</sub> O <sub>4</sub>	180	10	34	3	23	1.722	814.58
ZnLa <sub>0.5</sub> Fe <sub>1.5</sub> O <sub>4</sub>	180	12	16	0.3	153	0.811	2550
ZnFe <sub>2</sub> O <sub>4</sub>	180	12	13	0.3	32	0.562	433.33
ZnLa <sub>0.5</sub> Fe <sub>1.5</sub> O <sub>4</sub>	180	13	4.7	0.1	157	0.238	768.64
ZnLa <sub>0.5</sub> Fe <sub>1.5</sub> O <sub>4</sub>	170	12	35	1.2	46	1.772	1667.80
ZnLa <sub>0.5</sub> Fe <sub>1.5</sub> O <sub>4</sub>	200	12	16.5	0.46	165	0.836	2835.9

$$n_B = \frac{M \times M_S}{N \times \beta}, \quad (3)$$

where  $M$  is the molecular weight,  $N$  is the Avogadro's number and  $\beta$  is the conversion factor to express the magnetic moment per atom in Bohr magnetons (it value is  $9.27 \times 10^{-21}$  erg/Gauss). The obtained values of  $n_B$  are given in Table 2. It was clear that  $n_B$  varies similar to  $M_S$ , and this was considered as an indicator of the total magnetization for the samples [35, 36].

The anisotropy constant  $K$  can be evaluated using the following equation [35, 36]. The obtained values of  $K$  are listed in Table 3:

$$H_C = \frac{0.96K}{M_S}. \quad (4)$$

Results showed that the values of anisotropy constants ( $K$ ) for the samples  $\text{ZnLa}_{0.5}\text{Fe}_{1.5}\text{O}_4$  increase with the temperature increasing. The anisotropy constants of the nanoparticles depend on the crystallite size [40]. It ( $K$ ) increases with the temperature increasing (as the crystallite size increases with the temperature) due to minimization of the surface effect. The value of  $K$  for the samples  $\text{ZnLa}_{0.5}\text{Fe}_{1.5}\text{O}_4$  and  $\text{ZnFe}_2\text{O}_4$ , our result for un-doped sample was small comparable to the  $\text{La}^{3+}$  doped samples. It may be surface effect and cation distribution combined effects of value  $K$ .

## 4 Conclusion

$\text{ZnLa}_{0.5}\text{Fe}_{1.5}\text{O}_4$  nanoparticles were synthesized by hydrothermal method with different reaction conditions, including reaction temperature and reaction holding time, which causes appreciable changed in the structural and magnetic properties. The lattice constant and crystallite size were dependent for the samples with holding time and temperature. The lattice constant and crystallite size for the samples decreased with the increase of holding time at 180 °C. The lattice constant of the samples decreased with the temperature increasing, while the crystallite size increased with the temperature increasing. The magnetic properties were influenced surface effect for the samples at different holding times and temperatures. Anisotropy constant increases with the increasing of crystallite size, and it increased with the temperature increasing.

**Funding** This work were supported by the planned Science and Technology project of Hunan Province, China (2016TP1028) and supported by the double first-class discipline construction program of Hunan province.

## References

1. M.A. Mashhadi, A. Ramazani, S.J. Tabatabaei, H. Niknejad, Design and construction of multifunctional hyperbranched polymers coated magnetite nanoparticles for both targeting magnetic resonance imaging and cancer therapy. *J. Colloid Interface Sci.* **490**, 64–73 (2017)
2. P.F. Chen, H. Song, S. Yao, X. Tu, M. Su, Magnetic targeted nanoparticles based on  $\beta$ -cyclodextrin and chitosan for hydrophobic drug delivery and a study of their mechanism. *RSC. Adv.* **46**, 29025–29034 (2017)
3. J.H. Gao, H. Gu, B. Xu, ChemInform abstract: multifunctional magnetic nanoparticles: design, synthesis and biomedical applications. *Prog. Chem.* **42**, 1097–1107 (2011)
4. G. Unsoy, R. Khodadust, S. Yalcin, P. Mutlu, U. Gunduz, Synthesis of doxorubicin loaded magnetic chitosan nanoparticles for pH responsive targeted drug delivery. *Eur. J. Pharm. Sci.* **62**, 243–250 (2014)
5. W. He, H. Hosseinkhani, P. Hong, C. Chiang, D. Yu, Magnetic nanoparticles for imaging technology. *Int. J. Nanotechnol.* **10**, 930–944 (2013)
6. O.L. Gobbo, K. Sjaastad, M.W. Radomski, Y. Volkov, A. Primamello, Magnetic nanoparticles in cancer theranostics. *Theranostics.* **5**, 1249–1263 (2015)
7. P.A. Rose, P.K. Praseetha, M. Bhagat, P. Alexander, S. Abdeen, Drug embedded PVP coated magnetic nanoparticles for targeted killing of breast cancer cells. *Technol. Cancer Res. Treat.* **12**, 463–472 (2013)
8. M. Abbas, B.P. Rao, M.N. Islam, K.W. Kim, S.M. Naga, Size-controlled high magnetization  $\text{CoFe}_2\text{O}_4$  nanospheres and nanocubes using rapid one-pot sonochemical technique. *Ceram.Int.* **40**, 3269–3276 (2014)
9. J. Xie, C. Yan, Y. Zhang, N. Gu, Shape evolution of “multi-branched” Mn–Zn ferrite nanostructures with high performance: a transformation of nanocrystals into nanoclusters. *Chem. Mater.* **25**, 3702–3709 (2013)
10. ÂL. Andrade, M.A. Valente, J.M.F. Ferreira, J.D. Fabris, Preparation of size-controlled nanoparticles of magnetite. *J. Magn. Magn. Mater.* **324**, 1753–1757 (2012)
11. S.U. Haque, K.K. Saikia, G. Murugesan, S. Kalainathan, A study on dielectric and magnetic properties of lanthanum substituted cobalt ferrite. *J. Alloy. Compd.* **701**, 612–618 (2017)
12. S. Moise, E. Céspedes, D. Soukup, J.M. Byrne, A.J. Ei-Haj, The cellular magnetic response and biocompatibility of biogenic zinc-and cobalt-doped magnetite nanoparticles. *Sci. Rep. UK* **7**, 39922–39932 (2017)
13. A.S. Ahmed, R.V. Ramanujan, Magnetic field triggered multicycle damage sensing and self-healing. *Sci. Rep. UK* **5**, 13773–13782 (2015)
14. M. Mahdavi, M.B. Ahmad, M.J. Haron, F. Namvar, B. Nadi, Synthesis, surface modification and characterization of biocompatible magnetic iron oxide nanoparticles for biomedical applications. *Molecules.* **18**, 7533–7548 (2013)
15. X. Chu, J. Yu, Y.L. Hou, Surface modification of magnetic nanoparticles in biomedicine. *Chin. Phys. B.* **24**, 1–8 (2015)
16. R. Zhang, L. Sun, Z.D. Wang, W.T. Hao, E.S. Cao, Y.J. Zhang, Dielectric and magnetic properties of  $\text{CoFe}_2\text{O}_4$  prepared by sol-gel auto-combustion method. *Mater. Res. Bull.* **98**, 133–138 (2018)
17. L. Yang, G. Xi, T. Lou, X. Wang, J. Wang, Preparation and magnetic performance of  $\text{Co}_{0.8}\text{Fe}_{2.2}\text{O}_4$  by a sol-gel method using cathode materials of spent Li-ion batteries. *Ceram. Int.* **42**, 1897–1902 (2016)
18. M.A. Mashhadi, A. Ramazani, R.S.J. Tabatabaei, H. Niknejad, Design and construction of multifunctional hyperbranched polymers coated magnetite nanoparticles for both targeting magnetic

- resonance imaging and cancer therapy. *J. Colloid Interface Sci.* **490**, 64–73 (2017)
19. J. Xie, C. Yan, Y. Yan, L. Chen, Y. Zhang, Multi-modal Mn-Zn ferrite nanocrystals for magnetically- induced cancer targeted hyperthermia: a comparison of passive and active targeting effects. *Nanoscale*. **8**, 16902–16915 (2016)
  20. J. Xie, Y. Zhang, C.Y. Yan, L. Song, S. Wen, F.C. Zang, G. Chen, High-performance PEGlated Mn–Zn ferrite nanocrystals as passive-targeted agent for magnetically induced cancer theranostics. *Biomaterials* **35**, 9126–9136 (2014)
  21. N. Stocke, P. Sethi, A. Jyoti, R. Chan, A.M. Arnold, J.Z. Hilt, M. Upreti, Toxicity evaluation of magnetic hyperthermia induced by remote actuation of magnetic nanoparticles in 3D micrometastatic tumor tissue analogs for triple negative breast cancer. *Biomaterials*. **120**, 115–125 (2017)
  22. S. Kuai, Z. Nan, Formation mechanism of monodisperse Ce<sup>3+</sup> substituted ZnFe<sub>2</sub>O<sub>4</sub> nanoparticles. *J. Alloy. Compd.* **602**, 228–234 (2014)
  23. E. Ateia, M.A. Ahmed, A.K. EI-Aziz, Effect of rare earth radius and concentration on the structural and transport properties of doped Mn–Zn ferrite. *J. Magn. Magn. Mater.* **311**, 545–554 (2007)
  24. R. Pandey, L.K. Pradhan, M. Kar, Structural, magnetic, and electrical properties of (1 – x)Bi<sub>0.85</sub>La<sub>0.15</sub>FeO<sub>3–(x)}</sub> CoFe<sub>2</sub>O<sub>4</sub> multiferroic composites. *J. Chem. Solids*. **115**, 42–48 (2018)
  25. M. Hashim, S.E. Alimuddin, S. Shirsath, R. Kumar, Preparation and characterization chemistry of nano- crystalline Ni–Cu–Zn ferrite. *J. Alloy. Compd.* **549**, 348–357 (2013)
  26. V. Chaudhari, S.E. Shirsath, M.L. Mane, R.H. Kadam, S.B. Shelke, Crystallographic, magnetic and electrical properties of Ni<sub>0.5</sub>Cu<sub>0.25</sub>Zn<sub>0.25</sub>La<sub>x</sub>Fe<sub>2–x</sub>O<sub>4</sub> nanoparticles fabricated by sol-gel method. *J. Alloy. Compd.* **549**, 213–220 (2013)
  27. P.H. Hao, X.L. Mao, Y. Yang, B.S. Zhang, Influences of sintering time on phase, structure and microstructure of zircon. *J. Wuhan Univ. Technol.* **36**, 18–21 (2014)
  28. L. Zhao, H. Yang, L. Yu, Y. Cui, X. Zhao, Magnetic properties of re-substituted Ni–Mn ferrite nanocrystallites. *J. Mater. Sci.* **42**, 686–691 (2007)
  29. P.W. Voorhees, The theory of Ostwald ripening. *J. Stat. Phys.* **38**, 231–252 (1985)
  30. L. Kumar, M. Kar, Effect of La<sup>3+</sup> substitution on the structural and magnetocrystalline anisotropy of nanocrystalline cobalt ferrite (CoFe<sub>2–x</sub>La<sub>x</sub>O<sub>4</sub>). *Ceram. Int.* **38**, 4771–4782 (2012)
  31. R.S. Yadav, J. Havlica, P. Ptacek, I. Kuritka, Structural and magnetic properties CoFe<sub>2</sub>O<sub>4</sub> nanoparticles synthesized by starch-assisted sol-gel auto-combustion method in air, argon, nitrogen, and vacuum atmospheres. *J. Supercond. Nov. Magn.* **28**, 249–258 (2015)
  32. M.A. Amer, T. Meaz, M. Yehia, S.S. Attalah, F. Fakhry, Characterization, structural and magnetic properties of the as-prepared Mg-substituted Cu-nanoferrites. *J. Alloy. Compd.* **633**, 449–455 (2015)
  33. S.A. Saafan, T.M. Meaz, E.H. EI-Ghazzawy, M.K. Einimr, M.M. Ayad, M. Bakr, AC and DC conductivity of NiZn ferrite nanoparticles in wet and dry conditions. *J. Magn. Magn. Mater.* **322**, 2369–2374 (2010)
  34. E.H. EI-Ghazzawy, M.A. Amer, Structural, elastic and magnetic studies of the as-synthesized Co<sub>1–x</sub>Sr<sub>x</sub>Fe<sub>2</sub>O<sub>4</sub> nanoparticles. *J. Alloy. Compd.* **690**, 293–303 (2017)
  35. M.A. Amer, T.M. Meaz, S.S. Attalah, A.I. Ghonim, Structural and magnetic characterization of the Mg<sub>0.2–x</sub>Sr<sub>x</sub>Mn<sub>0.8</sub>Fe<sub>2</sub>O<sub>4</sub> nanoparticles. *J. Magn. Magn. Mater.* **363**, 60–65 (2014)
  36. A. Loganathan, K. Kumar, Effects on structural, optical, and magnetic properties of pure and Sr-substituted MgFe<sub>2</sub>O<sub>4</sub> nanoparticles at different calcination temperatures. *Appl. Nanosci.* **6**, 629–639 (2016)
  37. T.M. EI-Alaily, M.K. EI-Nimr, S.A. Saafan, M.M. Kamel, T.M. Meaz, Construction and calibration of a low cost and fully automated vibrating sample magnetometer. *J. Magn. Magn. Mater.* **386**, 25–30 (2015)
  38. P. Kunar, S.K. Sharma, M. Knobel, M. Singh, Effect of La<sup>3+</sup> doping on the electric, dielectric and magnetic properties of cobalt ferrite processed by co-precipitation technique. *J. Alloy. Compd.* **508**, 115–118 (2010)
  39. R. Peelamedu, C. Grimes, D. Agrawal, R. Roy, P. Yadoji, Ultralow dielectric constant nickel–zinc ferrites using microwave sintering. *J. Mater. Res.* **18**, 2292–2295 (2003)
  40. W.S. Chiu, S. Radiman, S. Abd-Shukor, M.H. Abdullah, P.S. Khiew, Tunable coercivity of CoFe<sub>2</sub>O<sub>4</sub> nanoparticles via thermal annealing treatment. *J. Alloy. Compd.* **459**, 291–297 (2008)

**Publisher's Note** Springer Nature remains neutral with regard to jurisdictional claims in published maps and institutional affiliations.